International Journal of Heat and Mass Transfer 143 (2019) 118444

Contents lists available at ScienceDirect

International Journal of Heat and Mass Transfer

journal homepage: www.elsevier.com/locate/ijhmt

Measurements and predictions of thermophoretic soot deposition

Amy E. Mensch *, Thomas G. Cleary

National Institute of Standards and Technology, 100 Bureau Drive, MS-8664, Gaithersburg, MD 20899, United States

ARTICLE INFO

Article history:
Received 15 February 2019
Received in revised form 15 July 2019
Accepted 17 July 2019

Keywords:
Soot deposition
Thermophoretic deposition
Deposition velocity

ABSTRACT

A thin laminar flow channel with a transverse temperature gradient was used to examine thermophoretic deposition of soot aerosol particles in experiments and modeled in Fire Dynamics Simulator (FDS) simulations. Conditions investigated included three flowrates, with nominal Reynolds number based on the hydraulic diameter of 55, 115 and 230, and two applied temperature gradients, nominally 10 °C/mm and 20 °C/mm, with repeats. Soot was generated from a propene diffusion flame. The burner exhaust was mixed with dilution air, and most large agglomerates greater than 1 μm aerodynamic diameter were removed prior to the channel inlet. The expected thermophoretic velocity of the aerosol was calculated from the applied temperature gradient. A calculated deposition velocity was determined from the mass of deposition, the channel inlet soot concentration, and the exposure time. Uniform soot deposition allowed targets to be used to measure the mass of deposition on the cold side of the channel. The mass of deposition was also determined by subtracting the mass of soot exiting the channel from the mass of soot entering the channel during the exposure time. The deposition velocities from these two methods generally agreed with the thermophoretic velocity and with each other. The deposition mass predicted by the FDS model also compared well with the experiments in most cases. The disagreements for the lowest flow rate cases are attributed to buoyant flow effects adding uncertainty to the actual temperature gradients present in the channel. (The opinions, findings, and conclusions expressed in this paper are the authors' and do not represent the views or policies of NIST or the United States Government.)

Published by Elsevier Ltd.

1. Introduction

Understanding the deposition of soot particles in a fire environment is of interest in fire forensics because of the role of soot deposition in burn pattern generation. Soot deposition is of interest in fire modeling because deposition acts as a sink in tracking the transport of soot, allowing predictions of smoke levels in a building fire. Smoke level predictions impact life safety predictions and potential for safe egress.

Soot from fires is an aerosol that can deposit on surfaces due to gravitational settling, diffusive and turbulent transport, and thermophoresis. Although soot aerosols can have a net electric charge, there is negligible electric field to cause electrostatic deposition in most fire scenarios. Gravitational settling is significant for large particles on the order of 10 μm or larger aerodynamic diameter [1], as their gravitational force compared to air resistance is more significant than for smaller particles. Deposition from turbulent flow, typically more significant than Brownian diffusion, occurs when turbulent eddies bring particles near a surface, and the particles tend to deposit due to direct interception by the surface or their inertia causing an impact with the surface.

Thermophoresis is the motion of aerosol particles in the direction of the surrounding gas temperature gradient. While convective transport usually dominates particle motion in the middle of an enclosure, thermophoresis becomes important in the low-velocity regions near the walls. The walls are normally at a relatively cooler temperature than the gases from the fire, so a temperature gradient is present. These factors result in thermophoretic deposition being a significant contributor to deposition in fires, particularly for small particles (0.1–1 μm) produced during flaming combustion [2].

Thermophoretic deposition is characterized by the thermophoretic velocity, v_{th}, which is the particle terminal velocity resulting from the temperature gradient in the gas, ∇T. Eq. (1) defines v_{th} as proportional to, but in the opposite direction of, ∇T, as well as a function of the gas viscosity, μ, the gas density, ρ, the temperature of the particle, T_p, and a thermophoretic coefficient, K_{th}.

$$v_{th} = -K_{th}\frac{\mu \nabla T}{\rho T_p} \tag{1}$$

* Corresponding author.
E-mail addresses: amy.mensch@nist.gov (A.E. Mensch), thomas.cleary@nist.gov (T.G. Cleary).

https://doi.org/10.1016/j.ijheatmasstransfer.2019.118444
0017-9310/Published by Elsevier Ltd.

The commonly used correlation for K_{th} depends on the Knudsen number (Kn, the ratio of the gas molecular mean free path to the characteristic length of the particle), the ratio of thermal conductivities of the gas and particle, and constants [3]. In the free molecular regime, when the particle is much smaller than the mean free path of the gas (Kn $\ll$ 1), K_{th} is estimated to be 0.55 and independent of particle size under those conditions [4].

Studies of soot agglomerates have found that thermophoresis depends mostly on the primary particle diameter [4–6], regardless of overall particle size, because thermophoresis is a surface phenomenon. The primary particle size of soot is in the range of 20–40 nm [7] and in the free molecular regime, resulting in a K_{th} of 0.55. Suzuki et al. [6] measured K_{th} to be between about 0.2 and 0.55 for soot agglomerates. The range in values suggested that K_{th} also depends on the morphological characteristics of the agglomerate particles, with open structures showing thermophoretic results closer to the free molecular regime compared to compact structures. Soot agglomerates from diffusion flames tend to have a more open structure characterized by a fractal dimension of 2 or less [7]. Recent theoretical studies suggest that K_{th} may depend on the number of primary particles, and therefore on agglomerate size, due to inter-particle momentum shielding [8].

The Fire Dynamics Simulator (FDS), a computational fluid dynamics code for fire prediction, calculates thermophoretic deposition, turbulent deposition and gravitational settling of aerosols [1,9,10] according to literature models, but there are limited experimental data available to assess the performance of the predictions. A model validation case requires accurate measurements of the soot deposition and the surrounding conditions, such as spatial and temporal variations in temperature, velocity, and soot concentrations, which can be difficult to obtain in fire experiments.

A possible way to measure the soot deposition and the required surrounding conditions is to design an experiment in a rectangular channel with a well-defined flow and a transverse temperature gradient to induce thermophoretic deposition on the cold side of the channel, such as in Messerer et al. [4]. If the flow is laminar, turbulent deposition can be neglected. If the channel is positioned vertically, gravitational settling can be neglected. Instead of directly measuring the v_{th}, as Suzuki et al. [6] did using image velocimetry, the overall deposition velocity, v_{dep}, can be calculated based on a mass balance. Tsai and Lu [11] solve for the penetration efficiency, η, defined as the fraction of the inlet concentration, C_{inlet}, that exits the channel for thermophoretic deposition in a parallel plate configuration with a parabolic flow profile.

$$\eta = 1 - \frac{C_{outlet}}{C_{inlet}} = \frac{v_{dep} L}{v_{ave} H}, \tag{2}$$

where C_{outlet} is the outlet concentration, v_{ave} is the average velocity along the channel, L is the channel length, and H is the channel height. From a mass balance, the mass loading of deposition, ML (the mass of deposition, m_{dep}, divided by the exposure area, L times channel width, W) is

$$\mathrm{ML} = \frac{(C_{inlet} - C_{outlet}) v_{ave} H W t}{L W}, \tag{3}$$

where t is the exposure time. Solving Eq. (3) for v_{ave} and substituting into Eq. (2) gives

$$v_{dep} = \frac{\mathrm{ML}}{C_{inlet} t}. \tag{4}$$

The v_{dep} can be directly compared to v_{th} if: v_{th} is uniform, thermophoresis is the dominant deposition mechanism (diffusion is negligible), the flow is steady and parallel to the deposition surface, the C_{inlet} is steady, and the local soot concentration above the wall does not drop significantly. Eq. (4) shows calculating v_{dep} requires measurement of the ML, t, and C_{inlet}. In this study, the v_{dep} is measured and compared to the expected v_{th} based on the measured temperature gradient. FDS simulations are also conducted to predict v_{dep}, and this is compared to the experimental results for model validation.

2. Experimental methods

The mechanism behind thermophoretic deposition was studied by introducing the diluted exhaust from a laminar propene diffusion flame into a thin rectangular laminar flow channel with a transverse temperature gradient applied across the channel height. The experimental apparatus is pictured in Fig. 1. The channel was positioned so the flow was vertically downward to remove the effect of gravitational deposition on the walls. Aluminum foil targets attached to the interior of the cold side of the channel allowed gravimetric measurement of deposited soot (the change in mass of the targets before and after exposure). The internal dimensions of the channel along with the hot and cold side walls are shown in Fig. 2 with the flow entering the inlet on the left of Fig. 2, passing through the inlet plenum, rectangular channel with temperature gradient, and then outlet plenum on the right of Fig. 2. The dimensions of the inlet plenum are shown in Fig. 2, and the outlet plenum is the same size. The plenums help to reduce entrance and exit effects on the channel flow. Additionally, a 6.4 mm diameter rod was inserted across the width of the inlet plenum, 25.4 mm from the flow inlet, to diffuse the jet entering at the flow inlet. Immediately after the flow exited the outlet plenum, it passed through a filter to remove the soot remaining in the outlet flow.

The flow through the channel was generated by the house vacuum line. The flowrate was manually set by a needle valve and measured by a thermal anemometer type flowmeter downstream of the channel and channel exit filter. The flowmeter also measured the flow temperature and pressure and displayed the flowrate at standard conditions, defined as 101 kPa and 21 °C. The standard flowrates tested were 2.5 L/min, 5.0 L/min and 10.0 L/min, corresponding to mass flowrates of 0.05 g/s, 0.1 g/s and 0.2 g/s. In the rest of the document, the flowrates are referred to as 2.5 SLM, 5.0 SLM and 10.0 SLM. The cases with flows of 2.5 SLM and 5.0 SLM were repeated four times; the cases with 10.0 SLM were repeated three times. The relative combined expanded uncertainty (using a coverage factor of 2, 95% confidence level) in the standard flowrate was ±2%. The flow Reynolds number, Re, using the hydraulic diameter, D_h, and the average channel velocity, was nominally 55, 115 and 230 for the three flowrates and laminar for all cases. Laminar flow implied that turbulent deposition was not present in the experiments. Also, laminar flow ensured the temperature profile was linear across the channel in the z-direction, meaning the temperature gradient was uniform. Steady-state conjugate heat transfer simulations in Mensch and Cleary [12] showed that the velocity and temperature profiles for 10.0 SLM and a temperature difference of 200 °C were fully-developed by half the channel length, 205 mm. The entrance lengths to achieve fully developed profiles were shorter for lower flowrates and lower temperature differences.

2.1. Thermal measurement methods

The hot side of the channel was bounded by a 19.1 mm thick aluminum wall (thermal conductivity = 238 W/(m·K)). The hot wall was heated by two rectangular resistance heaters centered on the outer side of the hot wall with a 6.4 mm gap between them (Fig. 1(b)). Each heater was 304.8 mm long, 38.1 mm wide and 8 mm thick. The heaters operated with on-off control based on the temperature measured on the outer surface of the hot wall between the two heaters centered along the length. The set point

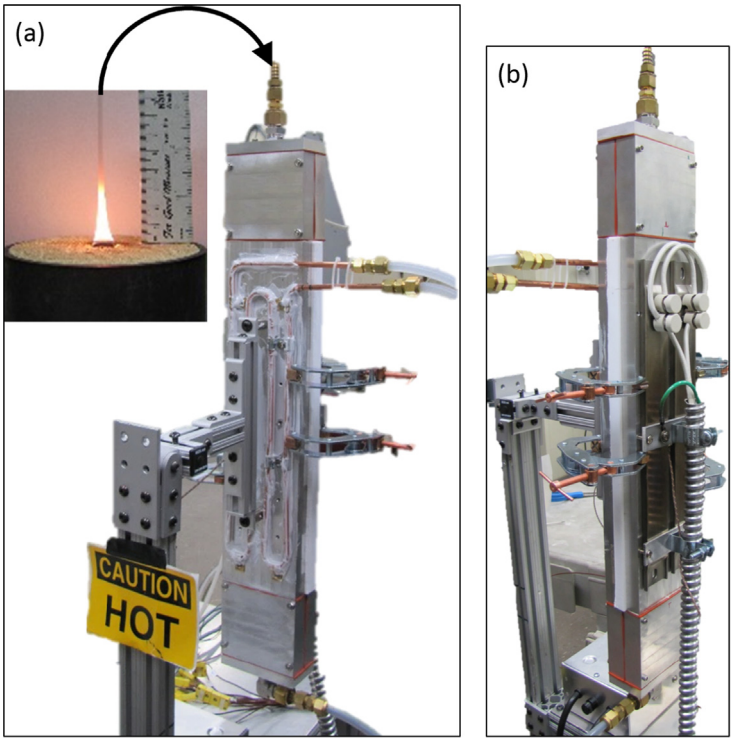

Fig. 1. Experimental apparatus showing (a) cold wall cooling circuit and (b) hot wall resistance heaters.

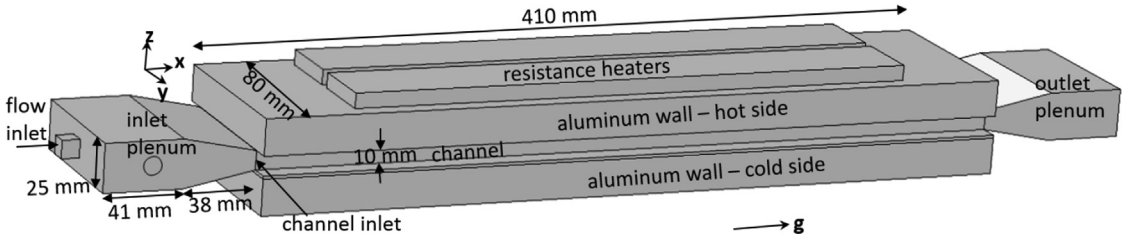

Fig. 2. Diagram of internal channel geometry and hot and cold side walls.

temperatures were 230 °C and 120 °C to generate cases with internal temperature differences of approximately 200 °C and 100 °C, respectively. The controller deadband was set to ±0.1 ° C, which resulted in standard deviations of 2.2 °C to 2.5 °C in the measured external wall temperature within each experiment.

The cold side of the channel was bounded by a thin layer (1.59 mm) of glass epoxy laminate circuit board material (thermal conductivity = 0.343 W/(m·K) across the thickness [13]). Outside of the glass epoxy boards was another aluminum wall, the same dimensions as the one on the hot side. The boards could be removed from the apparatus before and after experiments for careful preparation and handling of the delicate deposition targets. The Biot number, Bi, of the board was estimated to be less than 0.1. The cold aluminum wall was cooled by a serpentine copper line circulating cold water from the building supply (Fig. 1(a)). The temperature of the water was not controlled, but the temperature on the outer surface of the cold aluminum wall was measured during each test, with average temperatures ranging from 12 °C ± 0.6 °C to 21 °C ± 0.6 °C. The variation of the measured external wall temperature within each experiment was small, with standard deviations 0.1 °C to 0.8 °C. The other side walls were bounded by relatively low thermal conductivity polytetrafluoroethylene (thermal conductivity = 0.25 W/(m·K)) with a high temperature silicone gasket at the edges to reduce heat transfer between the hot and cold walls.

The internal temperature difference between the hot and cold surfaces was correlated to the external temperature difference because the internal temperature difference was not measured in experiments with soot exposure. The internal temperature difference was measured only for initial experiments without introducing soot into the flow. In the initial experiments, three K-type thermocouples (bead diameter of 0.025 mm) were adhered with polyimide tape to the interior hot and cold surfaces of the channel along the centerline. In eight temperature experiments, some conditions were repeated with the thermocouples in slightly different locations along the centerline. Additional variation in conditions was introduced by the temperature of the cold water and ambient conditions.

The differences between the hot and cold temperature at each location were averaged to give the average interior temperature difference, ΔT, for each set of conditions. The variation in internal ΔT between locations along the channel was at most ±5 % of the average. The interior ΔT and exterior ΔT were determined for all three nominal flowrates and for both set point temperatures. An overall linear correlation of average interior ΔT to external ΔT was established to be: $\Delta T_{interior}\,(^{\circ}\mathrm{C}) = 0.876\,[\Delta T_{exterior}\,(^{\circ}\mathrm{C})] + 2\,(^{\circ}\mathrm{C})$, with an R^2 correlation coefficient greater than 0.999. The combined expanded uncertainty in the $\Delta T_{interior}$ was ±4 °C. The expected ∇T in the channel was found by dividing $\Delta T_{interior}$ by the height of the channel, 10 mm.

The inlet and outlet flow temperatures were measured by K-type thermocouples in each plenum. In the case of the inlet plenum, the thermocouple was positioned just downstream of the cylindrical rod. The average of the inlet and outlet flow temperatures was used to calculate temperature dependent properties of the flow, such as viscosity, density, thermal conductivity and Kn. The average of the inlet and outlet flow temperatures was also used for T_p in Eq. (1). The channel flow temperatures required about 45 min to achieve steady-state, during which ambient air was pulled through the channel prior to soot exposure.

2.2. Soot Concentration measurement methods

Soot was generated by a laminar diffusion flame with propene as the fuel. The burner, which is pictured in Fig. 1(a), consisted of a 1.0 cm diameter tube for the fuel, surrounded by a 12.0 cm diameter ceramic honeycomb for the co-flow air [14]. The propene flowrate was 0.055 SLM, and the co-flow air flowrate was 54.1 SLM. The burner was enclosed by a brass chimney that contained a tripper plate to induce mixing followed by the injection of 32.5 SLM of additional dilution air. All fuel and air flowrates for the burner were set by mass flow controllers with a manufacturer reported uncertainty of ±1%.

Ten SLM of the flow exiting the burner was diverted for the experiments, while the rest was exhausted through a ceiling vent. The experimental flow passed through a cyclone separator, which had an aerodynamic diameter cutoff of 1 μm at a flow of 10 SLM. The aerodynamic diameter is defined as the equivalent diameter of a unit density sphere that has the same inertial characteristics of the real particle. The aerodynamic size distribution of the soot was measured after the cyclone by a micro-orifice low pressure cascade impactor. The results of two repeat experiments are shown in Fig. 3. From the log-probability plot, the mass median aerodynamic diameter was about 0.37 μm. A soot agglomerate with this aerodynamic diameter would contain tens of thousands of primary particles. From Fig. 3, about 27 % of the total mass of soot is in particles with aerodynamic diameters greater than 1 μm, owing to the fact that the size cutoff of the cyclone is not very sharp for soot agglomerates.

Next, there was a make-up line, which added or removed flow depending on the total amount of flow needed for the experiments. The total flow needed was double the flowrate through the channel because equal amounts passed through the channel and through a filter to measure the inlet concentration. For 5.0 SLM flows, no make-up flow was needed. For 2.5 SLM flows, 5.0 SLM was removed from the make-up line. For 10.0 SLM flows, 10.0 SLM was added through the make-up line. Due to the addition of clean air with the 10.0 SLM cases, a static inline mixer was added after the make-up injection. Then, the flow was evenly split with a y-shaped flow splitter. One side was connected to the channel inlet, and the other side was connected to the housing of a pre-weighed filter. A second thermal anemometer type flowmeter measured the flowrate through the inlet concentration filter to allow calculation of the channel inlet soot concentration, C_{inlet}.

Once the burner was lit and the chimney was assembled, the lines were simultaneously attached to the channel and inlet concentration filter, starting the exposure. The soot exposure to the channel and to the inlet concentration filter were the same, 30 min for 2.5 SLM and for 5.0 SLM, and 60 min for 10.0 SLM (due to the diluted soot concentration from the make-up flow). Once the lines were connected, the pressure in the line just after the channel exit was adjusted to ambient by partially closing off the flexible exhaust lines leading from the burner to the ceiling vent. This reduced leakage from the channel by keeping the channel pressure close to ambient. Soot exiting the channel was captured by another filter just after the pressure tap, and the mass deposited on that filter was used to estimate the soot concentration at the channel outlet. All filters were desiccated overnight to remove any accumulated water vapor prior to taking the mass measurement, both before and after exposure. The combined expanded uncertainties of C_{inlet} and C_{outlet} were 4% or less.

Mass loss corrections for the inlet and outlet filter concentrations were determined through experiments with no applied temperature gradient. The soot mass loss without a temperature gradient was measured for 15 min during six to eight experiments at each flowrate. The average mass loss was 0.9% for 2.5 SLM, 1.7% for 5.0 SLM, and 6.4% for 10.0 SLM. During these experiments, there was no observable deposit within the rectangular channel and no measurable mass detected on the aluminum targets in the channel. The mass losses from the burner to the plenum were assumed to be similar to the mass losses from the burner to the inlet filter because the tubing for the two paths was nearly identical in length

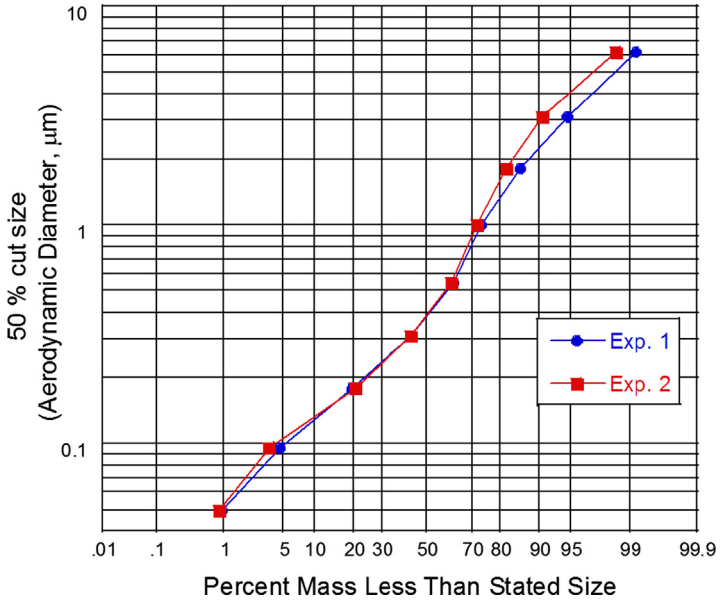

Fig. 3. Soot aerodynamic size distribution through cyclone separator.

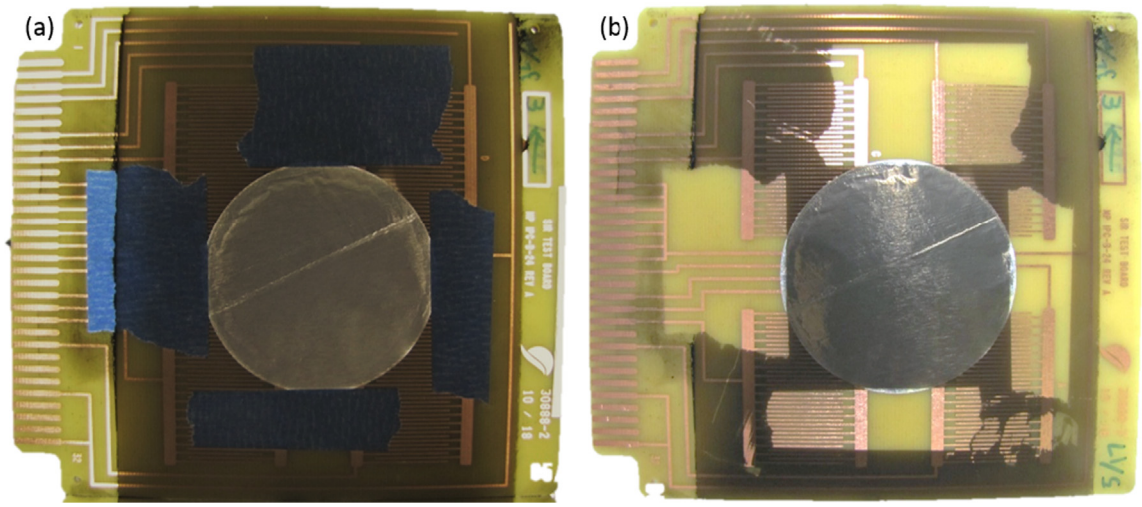

Fig. 4. Photographs of deposition on the FR-4 board and foil target for 0.055 SLM fuel flow, 3 SLM flow in channel, ΔT of 200 ° C, (a) before and (b) after tape removal.

and positioning. Therefore, the mass losses measured here were assumed to occur in the plenums, which did accumulate soot over time. As an approximation, the plenum mass loss percentage was assumed equal between the two plenums and divided by two. This estimate of the mass loss was subtracted from the measured C_{inlet} and added to the measured outlet soot concentration to determine the concentrations at the channel inlet and outlet planes.

It was also examined whether any non-soot particles, such as vapor condensation that could be off-gassed from heating the gasket material, were captured by the outlet concentration filter. This test case was performed twice for a nominal ΔT of 200 °C with ambient air entering the channel at 5.0 SLM. There was no measurable change in mass on the deposition targets in the channel. The additional concentration of non-soot particles, measured by the outlet concentration filter, resulted in an average $C_{non-soot}$ of 1.6 mg/m^3, at standard conditions. This value was subtracted from the outlet concentration measurement for experiments with nominal ΔT of 200 °C. The change in outlet concentration for a ΔT of 200 °C was only slightly greater than the uncertainty in the measurement. Since any off-gassing effect was expected to be reduced for a ΔT of 100 °C, the correction was not applied to ΔT of 100 °C cases.

2.3. Deposition measurement methods

The soot mass deposited is calculated in two different ways from independent measurements. The primary method is through gravimetric targets placed on the interior of the cold surface of channel. Four circular aluminum foil targets ($D = 47$ mm) were taped flush to the surface of the FR-4 boards. The targets were aligned along the center of the channel at 46 mm, 148 mm, 249 mm, and 351 mm from the channel inlet plane. After desiccating, the masses of the foil targets were measured before and after the deposition exposure. The change in mass was on the order of 0.05 mg for a nominal ΔT of 100 °C and on the order of 0.1 mg for a nominal ΔT of 200 °C. The uncertainty in each mass measurement was estimated as ±0.005 mg.

The approximate area of deposition was 1.69 E−3 m^2 ± 0.01 E−3 m^2, reflecting that 2% to 3% of the circular area was covered by tape. The deposit area was determined geometrically from photos, such as Fig. 4(b). Photos of an aluminum foil target on one of the FR-4 boards with soot exposure for a nominal ΔT of 200 °C is shown in Fig. 4 before and after removal of the tape. The photos in Fig. 4 also demonstrate the visible uniformity of soot deposition on the surface, which continued throughout all four boards along the channel. In some cases one target measured less mass than the others, but there was not a consistent trend among the experiments. The combined expanded uncertainty in gravimetric soot mass loading was calculated to be ±4 mg/m^2 for all cases. Typical mass loadings ranged from around 20 mg/m^2 to 60 mg/m^2.

The filter concentration measurements at the inlet and outlet of the channel were used to determine a second independent measurement of the deposited soot mass loading. The equation for the soot mass loading calculated from filter measurements, accounting for losses and non-soot particle corrections, is given in Eq. (5), where $\dot{V}_{outlet}$ is the volume flowrate of the channel outlet, and m_{outlet} is the mass deposited on the outlet filter. The deposit area, $A_{cold\ side}$, was 0.41 m × 0.080 m = 0.033 m^2. The combined expanded uncertainties in filter soot mass loading were found to be ±4.5 mg/m^2 for 2.5 SLM, ±8 mg/m^2 for 5.0 SLM, and ±14 mg/m^2 for 10.0 SLM.

$$\mathrm{ML}_{filter} = \left\{ [C_{inlet}(1 - \mathrm{loss}\,\%) + C_{non-soot}] \left(\dot{V}_{outlet} \right)(t) - m_{outlet} \right\} / A_{cold\ side} \tag{5}$$

The deposition velocities were calculated by dividing the soot mass loadings by the C_{inlet} and the total exposure time. The combined expanded uncertainty in gravimetric v_{dep} was about ±0.05 mm/s. For filter-based v_{dep}, the combined expanded uncertainty varied from case to case, but was often higher, as much as ±0.17 mm/s for the 10.0 SLM, ΔT of 200 °C case.

3. Flow and heat transfer modeling methods

Transient simulations to model the channel flow, heat transfer and soot deposition were conducted using FDS version 6.7.0 to obtain predictions for the soot deposition velocity. The aerosol deposition model in FDS treats soot as a gaseous species whose motion is influenced by not only the convective flow of the surrounding fluid, but also by the deposition mechanisms: gravitational, thermophoretic and turbulent [15]. Only the thermophoretic transport mechanism is activated in these simulations; gravitational and turbulent mechanisms are turned off. FDS applies an additional thermophoretic velocity based on the local temperature gradient to aerosol species located throughout the channel. FDS determines the thermophoretic velocity using Eq. (1) and correlations for K_{th}. FDS uses the local temperature in the cell for T_p and for the other temperature dependent properties needed to calculate K_{th} and v_{th}[16].

Table 1
Boundary conditions and parameters for FDS simulations.

	ΔT = 100 °C			ΔT = 200 °C		
Channel flow (SLM)	2.5	5.0	10.0	2.5	5.0	10.0
Ambient Pressure (Pa)	1.02 E5	1.03 E5	1.03 E5	1.01 E5	1.03 E5	1.02 E5
Average Channel Inlet Temperature (° C)	60.7	48.6	44.0	112.3	82.7	72.2
Inlet Volume Flowrate (Std. m^3/s)	3.96 E−5	8.01 E−5	1.58 E−4	3.89 E−5	7.97 E−5	1.57 E−4
Inlet Soot Mass Fraction (kg/kg)	5.94 E−5	5.72 E−5	2.29 E−5	5.97 E−5	5.56 E−5	2.21 E−5
Ambient Temperature (°C)	51.5	58.7	60.4	76.1	91.6	104.1
Cold Wall Temperature (°C)	18.2	18.3	14.0	20.7	22.5	19.3
Hot Wall Temperature (°C)	113.4	110.7	111.2	207.0	207.5	206.8

Table 2
Thermophoretic velocity calculation parameters and uncertainty.

	ΔT = 100 °C			ΔT = 200 °C		
Channel flow (SLM)	2.5	5.0	10.0	2.5	5.0	10.0
∇T (°C/mm)	9.50	9.45	9.79	18.83	18.70	18.93
T_p (° C)	48	50	51	77	81	93
v_{th} (mm/s)	0.29	0.29	0.30	0.61	0.60	0.62
Combined expanded uncertainty, v_{th} (mm/s)	0.01	0.01	0.02	0.01	0.01	0.05

The FDS default parameters were used for the soot species except for the particle size, which was changed to a diameter of 35 nm. This particle size ensured that the Kn was in the free molecular regime, which is expected for soot [6]. To model buoyancy, gravity is specified in the positive x-direction to match the experiments. The Direct Numerical Simulation (DNS) mode was employed for these simulations because the near wall temperature gradient was fully resolved with the selected grid resolution and laminar flow in the channel.

To simplify the computational domain, only the rectangular flow channel was modeled in FDS. The computational mesh was a structured rectangular grid with spacing of 2.5 mm across the length (x-direction) and width (y-direction), and 1 mm across the height (z-direction). Most of the flow and thermal boundary conditions were estimated based on the results of separate steady-state conjugate heat transfer simulations using Comsol,[1] which modeled the entire geometry in Fig. 2. The conjugate heat transfer simulations incorporated a mesh with both structured and unstructured elements, including wall-normal prism layers at the flow boundaries. A comprehensive description of the conjugate heat transfer simulations including boundary conditions is given in Mensch and Cleary [12].

A list of the boundary conditions applied for the six conditions is given in Table 1. The ambient pressure is an average of the ambient pressure measured on the dates experiments were taken with those conditions. The channel inlet temperature and velocity are specified for each grid cell on the channel inlet plane. The values for temperature and velocity are derived from the conjugate heat transfer simulation results. The average temperature across the channel inlet grid cells is given in Table 1 to show the trend of more upstream heating of the inlet flow for lower flowrates. This temperature is the same or higher than the temperature measured in the inlet plenum. The volume flowrate entering the channel in FDS is calculated (for standard conditions) from the inlet velocity and temperature distribution. The differences between the calculated inlet volume flowrates and the experimentally measured flowrates are 5% or less.

[1] Certain commercial equipment, instruments, or materials are identified in this paper in order to specify the procedures adequately. Such identification is not intended to imply recommendation or endorsement by the National Institute of Standards and Technology, nor is it intended to imply that the materials or equipment identified are necessarily the best available for the purpose.

The soot mass fraction specified for the channel inlet is calculated from the experimental measurements of inlet soot concentration with loss corrections, which are also given in Table 1. The ambient temperature, as specified in FDS, only has an influence at the channel outlet. Therefore, the ambient temperature is the average flow temperature at the channel outlet in the conjugate heat transfer simulations. Constant temperature boundary conditions are applied for the hot and cold walls because the conjugate heat transfer simulations showed that the temperature variation across these surfaces is minimal [12]. The cold and hot wall temperatures specified in FDS are the average surface temperatures found from the conjugate heat transfer simulations. The only other boundary conditions are adiabatic for the side walls made of polytetrafluoroethylene. The FDS simulations were run for 200 s, and in all cases, steady-state was achieved by 35 s.

4. Results and discussion

4.1. Expected thermophoretic velocities

The thermophoretic velocities, v_{th}, were calculated according to Eq. (1), and the associated measurements are given in Table 2. The temperature gradient in the channel, ∇T, was calculated by dividing the $\Delta T_{interior}$ by the channel height. T_p in Eq. (1) was approximated by averaging the flow temperatures measured at the inlet and outlet plenums, and viscosity and density were based on T_p. K_{th} was 0.55 for all cases, due to an assumed primary particle diameter of 35 nm, which kept the Kn above 4 and in the free molecular regime. The results for expected v_{th} and its combined expanded uncertainty are shown in Table 2.

4.2. Experimental deposition results

Table 3 reports the deposition results, averaged across the experiments at each condition. The results include C_{inlet} corrected for losses, the exposure time, the measured soot mass loadings, the deposition velocities calculated using Eq. (4), and the effective thermophoretic coefficient, K_{th}. The mass loadings, v_{dep}, and K_{th} are given for the primary gravimetric target method, averaged across all targets and experiment repeats, followed by the filter mass method, averaged across all experiment repeats. The effective K_{th} is calculated using Eq. (4) and the experimentally measured ∇T and T_p from Table 2. The average effective K_{th} is 0.47 for both the

Table 3
Experimental deposition measurements.

	ΔT = 100 °C			ΔT = 200 °C		
Channel flow (SLM)	2.5	5.0	10.0	2.5	5.0	10.0
C_{inlet} (mg/m^3)	66.3	64.6	23.6	61.2	58.6	23.5
Exposure time, t (s)	1800	1800	3600	1800	1800	3600
Gravimetric ML (mg/m^2)	25	28	24	57	62	47
$\sigma/\overline{ML}$ (within experiments)	15%	11%	12%	11%	9%	17%
Gravimetric v_{dep} (mm/s)	0.21 ± 0.05[a]	0.24 ± 0.04	0.25 ± 0.07	0.52 ± 0.09	0.59 ± 0.05	0.56 ± 0.05
Effective K_{th}	0.41	0.47	0.47	0.47	0.54	0.50
Filter ML (mg/m^2)	29	30	25	45	54	55
Filter v_{dep} (mm/s)	0.24 ± 0.04[a]	0.26 ± 0.13	0.26 ± 0.33	0.41 ± 0.10	0.51 ± 0.12	0.64 ± 0.43
Effective K_{th}	0.47	0.49	0.49	0.37	0.47	0.58
Channel deposition efficiency	18%	9%	5%	28%	18%	12%

[a] 2 σ

gravimetric and filter methods. This result is within the range of K_{th} measured by Suzuki et al. [6].

There is good agreement between the two distinct types of ML measurements, revealing that the soot mass was adequately accounted for in the various measurements and corrections. The standard deviation over the mean mass loading, $\sigma/\overline{ML}$, within experiments for the gravimetric targets is also reported to demonstrate the amount of scatter between the four target locations.

The standard deviation in both types of v_{dep} between the four experiments for 2.5 SLM and 5.0 SLM cases, and three experiments for 10.0 SLM cases is also reported. The gravimetric v_{dep} is based on the direct measurement of deposited soot, while the filter v_{dep} is derived from a difference between the soot entering and soot leaving the channel. The more direct measurement of the gravimetric v_{dep} explains the better repeatability (smaller σ) compared to the filter-based results. The gravimetric mass loading was generally uniform between the four targets measured in each experiment. The exception was that the first target in some ΔT = 200 °C cases measured slightly less than the other targets.

At the bottom of Table 3 is the channel deposition efficiency, or percentage of incoming soot that was deposited in the channel, based on the filter measurements. None of the channel deposition efficiencies are particularly high, which means that supply of soot was not greatly depleted to affect uniform deposition in the channel in any of the conditions examined.

4.3. FDS modeling results

The FDS deposition results are presented in Table 4. The first row reports C_{inlet} from the FDS results at the channel inlet, which are within 3% of the C_{inlet} in the experiments. Although the simulations were run for 200 s, the mass results from the simulations were scaled according to the same exposure times in the experiments, which are repeated in Table 4. The FDS ML was calculated using the predictions of soot mass deposited on four square areas on the cold wall surface to represent the gravimetric targets in the experiment. The square areas were centered at the locations of the targets in the experiment and had both dimensions equal to the diameter of the circular targets, 47 mm.

There are two deposition velocity calculations shown in Table 4, with the first, $v_{dep,in}$, using the FDS target ML and C_{inlet}, just as the gravimetric v_{dep} was calculated in the experiments. The second calculation, $v_{dep,loc}$, is an average of the local deposition velocities for 1 cm^2 areas covering the entire cold wall surface (328 locations). As reported in Mensch and Cleary [12], there is variation in the ML and v_{dep} in the upstream portion of the channel, but the deposition becomes uniform in the downstream half of the channel. The trends in deposition directly correspond to the changes in the temperature profile, which becomes fully-developed, linear and uniform by the downstream half of the channel. The local calculations used the local ML within the area, along with the local concentration just above the area. The $v_{dep,loc}$ is about the same or greater than $v_{dep,in}$ because FDS predicts some reduction in the local soot concentration, or supply of soot to be deposited, which is accounted for with $v_{dep,loc}$.

4.4. Comparison of results

All of the thermophoretic and deposition velocities from the experiments and FDS are plotted in Fig. 5. For clarity, the data for ΔT = 100 °C are offset slightly to the left, and the data for ΔT = 200 °C are offset slightly to the right. The measured and FDS deposition velocities show a strong dependence on the applied channel temperature gradient as expected. Additionally, the velocities at ΔT = 200 °C are approximately twice that of the velocities at ΔT = 100 °C, consistent with the temperature gradient dependence of Eq. (1).

The error bars in Fig. 5 represent the combined expanded uncertainties in the mean velocities. The error bars for the filter measurements (in green) are largest for the 10.0 SLM cases because those tests were run for twice as long and had more variability between experiments.

Most of the experimental conditions have measured and simulated deposition velocities that agree with the thermophoretic

Table 4
FDS Deposition results.

	ΔT = 100 °C			ΔT = 200 °C		
Channel flow (SLM)	2.5	5.0	10.0	2.5	5.0	10.0
FDS C_{inlet} (mg/m^3)	65.4	63.3	25.7	60.2	56.6	22.7
Exposure time, t (s)	1800	1800	3600	1800	1800	3600
FDS target ML (mg/m^2)	33	31	25	62	61	47
FDS $v_{dep,in}$ calculated with C_{inlet} (mm/s)	0.28	0.27	0.27	0.57	0.60	0.57
FDS $v_{dep,loc}$ calculated with local C (mm/s)	0.30	0.27	0.27	0.66	0.61	0.56

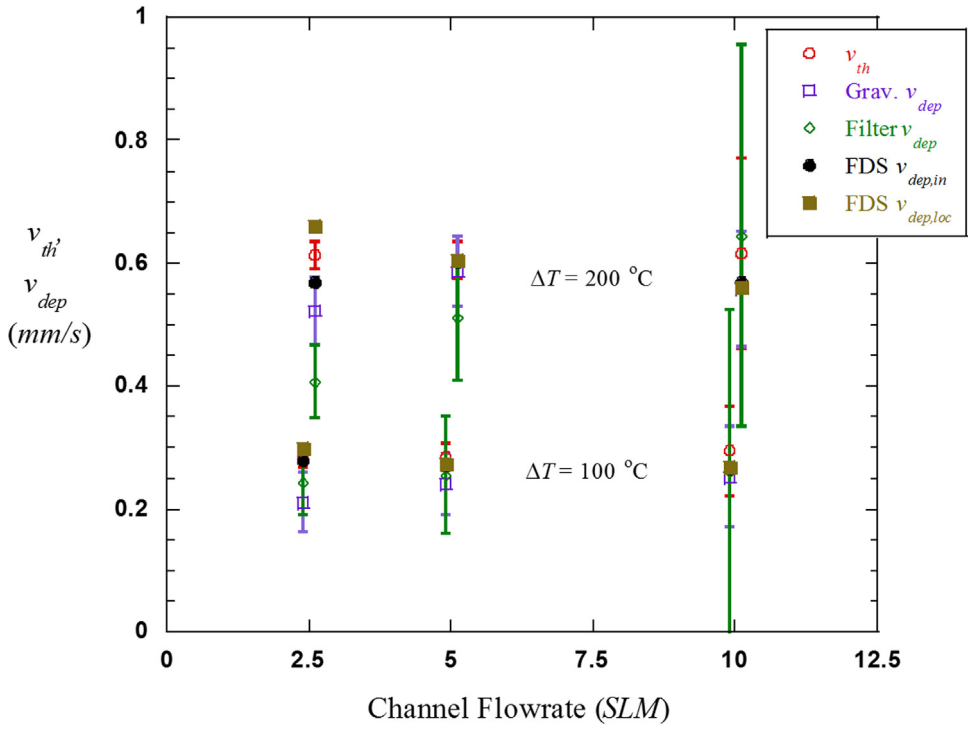

Fig. 5. Thermophoretic and deposition velocities and their uncertainties for each experimental condition.

velocities considering the uncertainties. The values of gravimetric v_{dep} agree with the expected v_{th} for all cases except at 2.5 SLM, where the error bars for gravimetric v_{dep} do not overlap with the error bars for v_{th}. The values of filter v_{dep} agree with the expected v_{th} for all cases except 2.5 SLM, ΔT = 200 °C, where the error bar for filter v_{dep} barely overlaps the error bar for v_{th}. The v_{dep} calculations from FDS results are within the experimental error of v_{th} for all the cases except 2.5 *SLM*, ΔT = 200 °C, where $v_{dep,in}$ is 0.02 mm/s lower than v_{th}, and $v_{dep,loc}$ is 0.03 mm/s greater than v_{th}.

To compare the results from the experiments and the simulations for validation purposes, the mass deposited, in terms of ML, is plotted in Fig. 6 to eliminate any effects of the assumed values

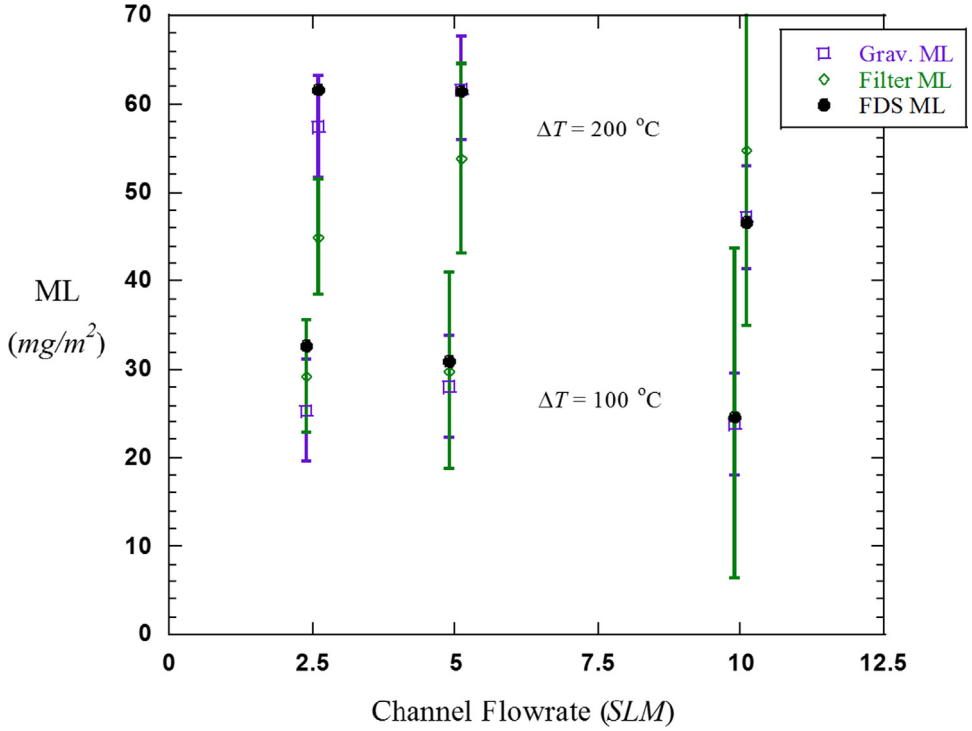

Fig. 6. Mass loading of soot deposition for each experimental condition (C_{inlet} and exposure times are given in Tables 3 and 4), along with th.e uncertainties.

of soot concentration. The values of ML are scaled to the exposure times in the experiments. For clarity, the data for ΔT = 100 °C are offset slightly to the left, and the data for ΔT = 200 °C are offset slightly to the right. The error bars are the combined expanded uncertainties in the mean ML. The two types of v_{dep} measurements have overlapping error bars for all cases except 2.5 SLM, ΔT = 200 °C, confirming the mass balance mentioned previously. The FDS predicted ML lies within the error bars for the gravimetric ML for all cases except at 2.5 SLM, ΔT = 100 °C. The FDS ML is also consistent with the filter ML for all cases except 2.5 SLM, ΔT = 200 °C.

Taking a closer look at the 2.5 SLM cases where there are differences, the experimental deposition results are all lower than the thermophoretic predictions and FDS predictions. The results are not expected to be dependent on flowrate, but the 2.5 SLM cases in particular experienced a unique flow feature that could have affected the temperature profiles and the soot deposition. At 2.5 SLM, and to a smaller extent at 5.0 SLM ΔT = 200 °C, reverse flow developed in the hotter half of the channel due to buoyancy. For the 2.5 SLM, ΔT = 200 °C case, FDS predicted reverse velocities of nearly 50% of the peak channel velocity in the main flow direction. While the inlet boundary conditions incorporated the reverse flow and upstream heating in the inlet velocity and temperature profiles, the matching between the experiments and predictions is worse when the buoyant effects are more pronounced.

The experimental temperature gradient present in the upstream portion of the channel also may be over-estimated for the 2.5 SLM cases, affecting the agreement between the measurements of v_{dep} and v_{th}. Evidence of upstream heating of the inlet flow was documented in the inlet temperature measurements in Ref. [12], and the inlet temperatures were highest for lower flowrates. An over-estimation of the overall temperature gradient in the upstream portion of the experimental channel would explain why the v_{dep} measurements are less than the expected v_{th}. In the gravimetric mass measurements, the first target had the lowest mass of deposited soot in three out of the four experiments at 2.5 SLM, ΔT = 200 °C. Meanwhile, FDS predictions showed the highest amounts of deposition toward the inlet of the channel, particularly for the 2.5 SLM cases.

5. Conclusion

Soot deposition measurements were conducted in a laminar flow channel with a transverse temperature gradient, and the deposition experiments were modeled in FDS simulations. Deposition velocities from two distinct experimental methods were compared to the expected thermophoretic velocities for two temperature gradients and three flowrates in multiple experiments with repeatable results. Agreement between the two types of deposition measurements showed that the soot mass was balanced among the inlet and outlet soot concentrations, the mass deposited on targets on the cold wall of the channel, and the mass loss corrections measured without a temperature gradient.

There was also overlap between the error bars for the v_{dep} measurements and the thermophoretic velocities (using K_{th} = 0.55), except for the 2.5 SLM cases, where the reverse flow due to buoyancy probably resulted in an over-estimation of the temperature gradient in the beginning of the channel. Most of the conditions represented good validation cases for the FDS deposition models for soot, while using a small value for particle size such as 35 nm used here. FDS predicted thermophoretic deposition in agreement with the gravimetric measurements for all cases except 2.5 SLM, ΔT = 100 °C, where there was a 5% difference from the mass loading prediction and gravimetric measurement. The issues with agreement for the 2.5 SLM cases were attributed to the unique flow development, which became less predominant when the channel flowrate was increased.

The measurements resulted in an average effective thermophoretic coefficient of 0.47, which is consistent with the results of Suzuki et al. [6] and close to the expected value of K_{th} = 0.55. The results are consistent with a recommendation of a constant K_{th} in the context of predicting thermophoretic soot deposition in fires.

Declaration of Competing Interest

There are no conflicts of interest involved in this paper or its contents.

Acknowledgements

We would like to thank Randall McDermott and Jason Floyd for their help with the FDS simulations and review of the paper. We also thank the anonymous reviewer for their thoughtful feedback. This work was funded through the National Institute of Standards and Technology, Engineering Laboratory.

References

[1] J. Floyd, K. Overholt, O. Ezekoye, Soot deposition and gravitational settling modeling and the impact of particle size and agglomeration, Fire Saf. Sci. 11 (2014) 376–388, https://doi.org/10.3801/IAFSS.FSS.11-376.

[2] K.M. Butler, G.W. Mulholland, Generation and transport of smoke components, Fire Technol. 40 (2) (2004) 149–176, https://doi.org/10.1023/B:FIRE.0000016841.07530.64. <http://link.springer.com/10.1023/B:FIRE.0000016841.07530.64>.

[3] J.R. Brock, On the theory of thermal forces acting on aerosol particles, J. Colloid Sci. 17 (8) (1962) 768–780, https://doi.org/10.1016/0095-8522(62)90051-X. <http://linkinghub.elsevier.com/retrieve/pii/009585226290051X>.

[4] A. Messerer, R. Niessner, U. Pschl, Thermophoretic deposition of soot aerosol particles under experimental conditions relevant for modern diesel engine exhaust gas systems, J. Aerosol Sci. 34 (8) (2003) 1009–1021, https://doi.org/10.1016/S0021-8502(03)00081-8. <http://www.sciencedirect.com/science/article/pii/S0021850203000818>.

[5] D.E. Rosner, Y.F. Khalil, Particle morphology- and knudsen transition-effects on thermophoretically dominated total mass deposition rates from "coagulation-aged" aerosol population, J. Aerosol Sci. 31 (3) (2000) 273–292, https://doi.org/10.1016/S0021-8502(99)00054-3. <http://www.sciencedirect.com/science/article/pii/S0021850299000543>.

[6] S. Suzuki, K. Kuwana, R. Dobashi, Effect of particle morphology on thermophoretic velocity of aggregated soot particles, Int. J. Heat Mass Transf. 52 (21–22) (2009) 4695–4700, https://doi.org/10.1016/j.ijheatmasstransfer.2009.05.017. <http://linkinghub.elsevier.com/retrieve/pii/S0017931009003421>.

[7] R.J. Samson, G.W. Mulholland, J.W. Gentry, Structural analysis of soot agglomerates, Langmuir 3 (2) (1987) 272–281, https://doi.org/10.1021/la00074a022. <http://pubs.acs.org/doi/abs/10.1021/la00074a022>.

[8] D.E. Rosner, P. Tandon, Knudsen transition effects on the thermophoretic properties of fractal-like aggregates: Implications for thermophoretic sampling of high-pressure flames, Aerosol Sci. Technol. 51 (11) (2017) 1262–1274, https://doi.org/10.1080/02786826.2017.1353061. <https://www.tandfonline.com/doi/full/10.1080/02786826.2017.1353061>.

[9] J. Floyd, R. McDermott, Modeling soot deposition using large eddy simulation with a mixture fraction based framework, in: Interflam: Proceedings of the 12th International Conference, Interscience Communications, 2010.

[10] J. Floyd, A numerical investigation on the impact of modeling aerosol behaviors on the prediction of soot density in a compartment fire, Interflam: Proceedings of the 14th International Conference, vol. 2, Interscience Communications, 2016, pp. 835–846.

[11] C.-J. Tsai, H.-C. Lu, Design and evaluation of a plate-to-plate thermophoretic precipitator, Aerosol Sci. Technol. 22 (2) (1995) 172–180, https://doi.org/10.1080/02786829408959738. <http://www.tandfonline.com/doi/abs/10.1080/02786829408959738>.

[12] A. Mensch, T. Cleary, A soot deposition gauge for fire measurements, NIST Technical Note 1985, Natl. Inst. Stand. Technol. (2018), https://doi.org/10.6028/NIST.TN.1985.

[13] F. Sarvar, N.J. Poole, P.A. Witting, PCB glass-fibre laminates: thermal conductivity measurements and their effect on simulation, J. Electron. Mater. 19 (12) (1990) 1345–1350, https://doi.org/10.1007/BF02662823. <http://link.springer.com/10.1007/BF02662823>.

[14] T.G. Cleary, G.W. Mulholland, L.K. Ives, R.A. Fletcher, J.W. Gentry, Ultrafine combustion aerosol generator, Aerosol Sci. Technol. 16 (3) (1992) 166–170, https://doi.org/10.1080/02786829208959546. <http://www.tandfonline.com/doi/abs/10.1080/02786829208959546>.

[15] K. McGrattan, S. Hostikka, R. McDermott, J. Floyd, M. Vanella, Fire Dynamics Simulator Technical Reference Guide Volume 1: Mathematical Model, NIST Special Publication 1018-1, National Institute of Standards and Technology, Gaithersburg, MD, 2018. doi:https://doi.org/10.6028/NIST.SP.1018. <https://nvlpubs.nist.gov/nistpubs/Legacy/SP/nistspecialpublication1018.pdf>.

[16] K. McGrattan, S. Hostikka, R. McDermott, J. Floyd, M. Vanella, Fire Dynamics Simulator User's Guide 6th Edition, Tech. Rep. NIST SP 1019, National Institute of Standards and Technology, Gaithersburg, MD, 2018. doi:https://doi.org/10.6028/NIST.SP.1019. URL <https://nvlpubs.nist.gov/nistpubs/Legacy/SP/nistspecialpublication1019.pdf>.